

Port hole perturbations to the magnetic field in MST

P J Fimognari¹, A F Almagri¹, J K Anderson¹, D R Demers², J S Sarff¹,
V Tangri¹ and J Waksman¹

¹ Department of Physics, University of Wisconsin-Madison, Madison, WI 53706, USA

² Rensselaer Polytechnic Institute, Troy, NY 12180, USA

E-mail: fimognari@wisc.edu

Received 26 February 2010, in final form 23 June 2010

Published 19 July 2010

Online at stacks.iop.org/PPCF/52/095002

Abstract

Axisymmetric magnetic equilibrium reconstruction is insufficient for describing several effects in the Madison Symmetric Torus (MST). Inclusion of the field error produced by port holes in the close-fitting conducting vacuum chamber enables accurate interpretation of data from several subsystems, in particular, ion trajectories of a heavy ion beam probe and radial displacement and distortion of power deposition from RF antenna heating. In this work, an analytic solution for the magnetic field error produced by a port hole is added to the equilibrium. Without inclusion, the beam trajectory can deviate by over a centimeter (on the order of the detector width) at the analyzer apertures. In addition, the deposition layer for an electron Bernstein wave is strongly altered up to one port diameter away from the port hole.

(Some figures in this article are in colour only in the electronic version)

1. Introduction

In this paper we analyze the perturbation of a port hole on the magnetic field in the Madison Symmetric Torus (MST) reversed-field pinch device. The primary motivation for this work has been to improve the accuracy of the ion beam trajectory simulation of the heavy ion beam probe (HIBP) [1, 2] through the MST plasma (MST) [3]. MST is a reversed-field pinch toroidal confinement device with a major radius of 1.5 m and a minor radius of 0.52 m, capable of operating at a plasma current of up to 600 kA. It has a 5 cm thick aluminum shell, with a number of small port holes for diagnostic access to the plasma. A HIBP measures quantities in the plasma interior by injecting a beam of singly charged heavy ions which are deflected by the confining magnetic field. A fraction of the beam is ionized to a doubly charged state, passes through an exit port and into an electrostatic energy analyzer. A 45 keV potassium ion beam through a MST discharge with a 380 kA peak plasma current and 4 kG equilibrium magnetic field is used as an example herein. Perturbations of the magnetic field must be accounted for

to accurately determine the beam path and the sample volume location. A second motivation for understanding the local magnetic perturbation due to a port hole is the coupling of RF antennas to the plasma. Electron Bernstein wave (EBW) deposition is strongly influenced, in that both the optimal launching frequency and deposition layer are altered by port field errors. In addition, probes affected by magnetic fields can benefit from a more precise accounting of the magnetic field in their immediate vicinity.

A magnetic field error is defined as any non-symmetric component of the local magnetic field. One source of magnetic field errors are perturbations in the flow of wall currents caused by diagnostic ports. A number of studies have considered the effect of magnetic field errors on particle transport and confinement [4–13]. Some have concentrated on studying the field errors within the plasma, as the control of these provides improvement to confinement. Fewer have considered the effect of a port field error. To date, the estimations or approximations of this issue have been largely concerned with the influence on the bulk plasma behavior, i.e. the far-field limit of the port field error [8–13]. Alternatively, it is advantageous to have a model that accurately predicts both the near- and far-field effects.

Detailed ion trajectory calculations are required to determine accurately the measurement sample volume for the HIBP. For systems where the magnetic field is determined primarily by magnet windings, this is straightforward and need only be performed each time major system parameters are changed. However, in MST, the magnetic field is largely generated by current within the plasma, and it is important to track the motion of the sample volume as it changes within a single discharge, between discharges, and in different plasma conditions. It is useful to be able to include corrections due to the port field error in the trajectory calculation, without having to do an FEM solution in addition to an equilibrium reconstruction for each set of conditions. An analytic solution meets this goal while also improving the computational time of the trajectory calculation, as it is more efficient than the storage and interpolation of large 3D arrays that would be necessary to determine the effect of the port field using computational solutions.

In all cases of MST operation, there is a large current that flows in the wall of the aluminum vacuum vessel. This current provides passive control of the plasma equilibrium position. A smaller driven wall current provides a weak toroidal field component. We treat the effect of the port hole as a perturbation to the otherwise axisymmetric magnetic field. Since the majority of the current in the wall is an image of the global plasma current in the core, this is a good approximation. While our focus here is the local perturbation of the magnetic field, the analytic solution presented below nevertheless provides an estimate of the perturbed vacuum magnetic field throughout the plasma volume. Analysis of magnetic island formation within the core plasma would require such an estimate (as well as analysis of the plasma response), but this topic is beyond the scope of this paper.

The primary assumptions behind the calculation presented below are as follows. First, the scale length of the equilibrium field near the port is larger than the port itself. Second the port radius is much smaller than the minor radius of the conducting shell, when the model is adjusted to the MST toroidal coordinate system. Finally, effects associated with perturbed plasma current are ignored, since the port hole error has negligible impact on the global current flowing in the plasma core. The magnetic field perturbation falls exponentially on a scale of the diameter of the port hole.

An outline of this paper is as follows. Section 2 develops the model in planar coordinates from the solution to a boundary-value problem and introduces a correction based on finite shell conductivity. Section 3 maps this solution to a toroidal coordinate system used on MST. Section 4 shows a comparison between the fourier decompositions of both the analytic solution and a finite element simulation. Section 5 validates the model against measurements taken

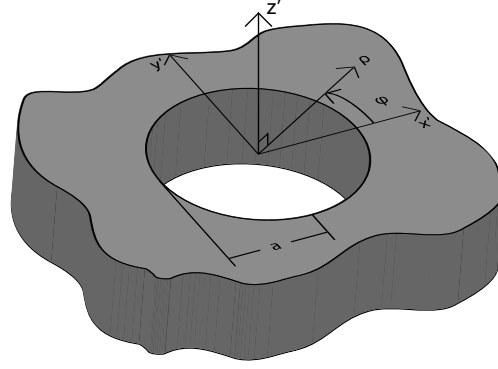


Figure 1. Planar solution geometry. A port with radius a located on a conducting plane. x' , y' and z' are orthonormal and originate at the center of the port, with $z' = 0$ as the delimiter between the uniform equilibrium magnetic field region and the conducting plane. ρ and ϕ are the radial and azimuthal coordinates with respect to the hole.

around a MST diagnostic port using a toroidal field. Section 6 shows the effect of the port field error on HIBP trajectory calculations. Section 7 describes the effect of the port field error on EBW optimal launch frequency and deposition layer. Section 8 provides the conclusions and summary of this paper.

2. Solution in plane geometry

This model starts from a boundary-value problem, solving for the effect of a circular hole in a perfectly conducting plane with a uniform magnetic field on one side. Figure 1 shows this geometry and a coordinate system which will be subsequently referred to as the port coordinate system. The slowly varying magnetic field has a magnitude of $B_0(t)$ and is taken to be oriented in the \hat{y}' direction. At any given time, the scalar magnetic potential in this case, following [14], is

$$\Phi_{\text{total}}(\mathbf{x}', t) = \begin{cases} -\frac{B_0(t) y'}{\mu_0} + \Phi^1(\mathbf{x}', t) & z' \geq 0, \\ -\Phi^1(\mathbf{x}', t) & z' < 0. \end{cases} \quad (1)$$

This potential satisfies Laplace's equation, and with the following boundary conditions,

$$\begin{aligned} \Phi_{\text{total}} \text{ continuous across } z = 0 & \quad \text{for } 0 \leq \rho < a, \\ \frac{\partial \Phi_{\text{total}}}{\partial z} = 0 \text{ at } z = 0 & \quad \text{for } a < \rho < \infty, \end{aligned} \quad (2)$$

the perturbation potential of the hole, Φ^1 , can be given in terms of Bessel functions $J_\nu(u)$, as

$$\Phi^1(\mathbf{x}', t) = \frac{2}{\pi} \frac{B_0(t)}{\mu_0} a^2 \sin(\varphi) \sqrt{\frac{\pi}{2}} \int_0^\infty J_{\frac{3}{2}}(ka) e^{-k|z'|} J_1(k\rho) \frac{dk}{k}. \quad (3)$$

Applying formula 6.752.4 in [15] gives a simplification of integrals of the general form of (3), and we find

$$\Phi^1(\mathbf{x}', t) = \frac{B_0(t)}{\mu_0} \frac{\rho \sin(\varphi)}{\pi} \left[-\frac{a}{l} \sqrt{1 - \left(\frac{a}{l}\right)^2} + \sin^{-1} \left(\frac{a}{l}\right) \right], \quad (4)$$

with l given by

$$l(x') = \frac{1}{2}(\sqrt{(a+\rho)^2 + (z')^2} + \sqrt{(a-\rho)^2 + (z')^2}). \quad (5)$$

The formulae for the perturbation magnetic field are then

$$\Delta B_{x'} = B_0(t) \operatorname{sgn}(z') \frac{x'y'}{\pi \rho l^4} \frac{a^3}{\sqrt{1 - \left(\frac{a}{l}\right)^2}} \times \left(\frac{a+\rho}{\sqrt{(a+\rho)^2 + (z')^2}} - \frac{a-\rho}{\sqrt{(a-\rho)^2 + (z')^2}} \right), \quad (6)$$

$$\begin{aligned} \Delta B_{y'} = B_0(t) \operatorname{sgn}(z') \frac{(y')^2}{\pi \rho l^4} \frac{a^3}{\sqrt{1 - \left(\frac{a}{l}\right)^2}} \times & \left(\frac{a+\rho}{\sqrt{(a+\rho)^2 + (z')^2}} - \frac{a-\rho}{\sqrt{(a-\rho)^2 + (z')^2}} \right) \\ & + B_0(t) \operatorname{sgn}(z') \frac{1}{\pi} \left(\frac{a}{l} \sqrt{1 - \left(\frac{a}{l}\right)^2} - \sin^{-1} \left(\frac{a}{l} \right) \right), \end{aligned} \quad (7)$$

and

$$\Delta B_{z'} = B_0(t) \operatorname{sgn}(z') \frac{y'z'}{\pi l^4} \frac{a^3}{\sqrt{1 - \left(\frac{a}{l}\right)^2}} \times \left(\frac{1}{\sqrt{(a+\rho)^2 + (z')^2}} + \frac{1}{\sqrt{(a-\rho)^2 + (z')^2}} \right). \quad (8)$$

In the above equations, the $\operatorname{sgn}(z')$ function is defined as

$$\operatorname{sgn}(z') = \begin{cases} +1 & z' \geq 0, \\ -1 & z' < 0. \end{cases} \quad (9)$$

While equations (6)–(8) are continuous for all space, there are several singularities when implementing this solution computationally; the behavior of the function at each of these locations can be determined. The \hat{x}' and \hat{y}' components are affected by two singularities, one which occurs when $l = a$, in other words, when $z' = 0$ and $\rho \leq a$. Then,

$$\Delta B_{x'} = 0 \quad (10)$$

and

$$\Delta B_{y'} = -\frac{1}{2} B_0(t). \quad (11)$$

The other singularity occurs when $\rho = 0$. In that case,

$$\Delta B_{x'} = 0 \quad (12)$$

and

$$\Delta B_{y'} = B_0(t) \operatorname{sgn}(z') \frac{1}{\pi} \left(\frac{a}{l} \sqrt{1 - \left(\frac{a}{l}\right)^2} - \sin^{-1} \left(\frac{a}{l} \right) \right). \quad (13)$$

When $z' = 0$ and $\rho \leq a$, as $a/l = 1$ in this situation, so $\Delta B_{z'}$ has an indeterminate value. For small z , we can expand (5) to give

$$l \approx a + \frac{(z')^2}{4} \left(\frac{1}{a+\rho} + \frac{1}{a-\rho} \right). \quad (14)$$

We can then write

$$\begin{aligned} \sqrt{1 - \left(\frac{a}{l}\right)^2} & \approx \sqrt{1 - \left(\frac{1}{1 + \frac{(z')^2}{4a} \left(\frac{1}{a+\rho} + \frac{1}{a-\rho} \right)} \right)^2} \\ & \approx \sqrt{1 - \left(1 - \frac{(z')^2}{4a} \left(\frac{1}{a+\rho} + \frac{1}{a-\rho} \right) \right)^2} \approx \frac{z'}{\sqrt{2a}} \sqrt{\frac{1}{a+\rho} + \frac{1}{a-\rho}}. \end{aligned} \quad (15)$$

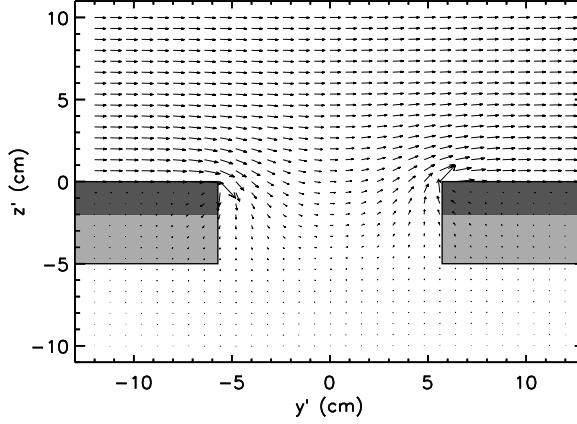


Figure 2. $B_{y'}$ and $B_{z'}$ vectors. The shaded region denotes the conducting shell, with the upper shaded region indicating the depth to which the field diffuses. One hundred plates were used to simulate the diffusion, spaced evenly from $z' = 0$ to $z' = -2$ cm. y' and z' are in the port coordinate system as defined in figure 1.

Inserting (15) into (8) gives

$$\Delta B_{z'} \approx B_0(t) \frac{y'}{\pi} \frac{2}{\sqrt{a^2 - \rho^2}}. \quad (16)$$

which has the correct behavior for the perturbation field to be continuous everywhere.

This solution is valid for a infinitely thin, perfectly conducting shell. In order to adapt it for the effect of diffusion of the field into an imperfect conductor, a linear superposition of a large number, N , of shells in the $-\hat{z}$ direction is used, with the field normalization for each plate falling off exponentially. This gives a total perturbation field of

$$\Delta B_u = \frac{\sum_{n=1}^N \Delta B_u(z' \rightarrow z' - z'_n) e^{z'_n/\delta}}{\sum_{n=1}^N e^{z'_n/\delta}}, \quad u \in \{x, y, z\}, \quad (17)$$

where δ is the shell skin depth. Figure 2 shows the vector plot of $B_{y'}$ and $B_{z'}$ vectors in the $x' = 0$ plane. Here, the port radius is 5.7 cm, the wall thickness is 5 cm and the skin depth is 0.4 cm (for a time scale of 2 ms in a 6063 aluminum shell, a typical time scale in MST). The Alfvénic time scale for a MST shot is on the order of $1 \mu\text{s}$, much smaller than the rate of change of the mean equilibrium field. These values are representative of the dimensions and conditions at the HIBP exit port on MST. The vector plot shows that at approximately one port diameter from the center of the port, the perturbation has dropped to a negligible level. It also suggests that beam trajectories passing near the edge of the port may experience a larger deflection due to the port field error than those passing near the center.

3. Approximation for toroidal geometry

To approximate the port field error in a toroidal device like MST, the toroidal and poloidal magnetic fields must be included. Here we solve the case for one circular port that is normal to the MST vessel, reflective of most MST ports (we could also approximate elliptical ports, or ports not orientated normal to the device surface with relative ease). This is accomplished by treating each component of the field separately and summing the resulting magnetic fields.

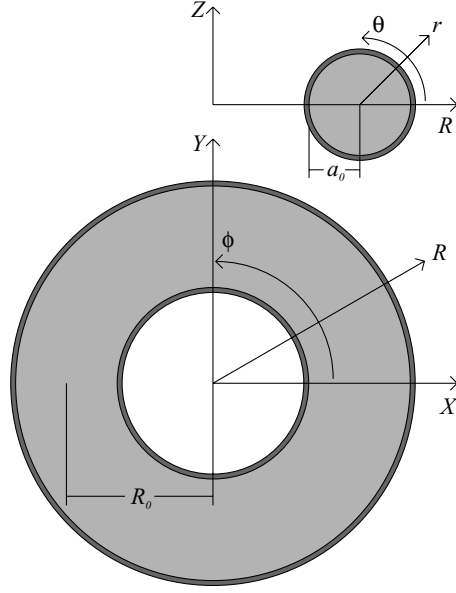


Figure 3. Top down (lower) and poloidal cross-section (upper) MST geometry in both Cartesian (X, Y, Z) and toroidal (R, ϕ, θ) coordinates. R_0 and a_0 are the major and minor radii of the torus.

Figure 3 shows the Cartesian and toroidal coordinate systems used to describe the geometry of MST. For the rest of this work, this coordinate system is denoted as MST coordinates.

The coordinate mapping necessary to approximate the perturbation due to a toroidally oriented equilibrium magnetic field near a port is given by

$$x' \rightarrow a_0(\theta - \theta_0), \quad (18)$$

$$y' \rightarrow (a_0 \cos(\theta) + R_0)(\phi - \phi_0), \quad (19)$$

$$z' \rightarrow r - a_0, \quad (20)$$

where R_0 and a_0 are the major and minor radii of MST and ϕ and θ are the toroidal and poloidal coordinates. We define the port to be located at (a_0, θ_0, ϕ_0) . This approximation is most accurate when the radius of the hole is much less than the minor radius of the device, as is the case for the diagnostic ports of MST. The largest ports on MST have a radius of 5.7 cm and are used by the HIBP and the EBW RF antenna. The coordinate mapping for a perturbation due to a poloidally oriented equilibrium magnetic field simply swaps the \hat{x}' and \hat{y}' coordinate transforms. Since the RFP equilibrium is helical, inclusion of toroidal and poloidal perturbations is necessary to describe the port effect. The sum of these gives

$$\Delta B_r = \Phi_0 \frac{r - a_0}{\pi l^4} \frac{a^3}{\sqrt{1 - \left(\frac{a}{l}\right)^2}} \left[\frac{1}{l_p} + \frac{1}{l_n} \right], \quad (21)$$

$$\begin{aligned} \Delta B_\theta = \Phi_0 \frac{a_0(\theta - \theta_0)}{\pi \rho l^4} \frac{a^3}{\sqrt{1 - \left(\frac{a}{l}\right)^2}} \left[\frac{a + \rho}{l_p} - \frac{a - \rho}{l_n} \right] \\ + \frac{B_{\theta_0}}{\pi} \operatorname{sgn}(r - a_0) \left[\frac{a}{l} \sqrt{1 - \left(\frac{a}{l}\right)^2} - \sin^{-1} \left(\frac{a}{l} \right) \right] \end{aligned} \quad (22)$$

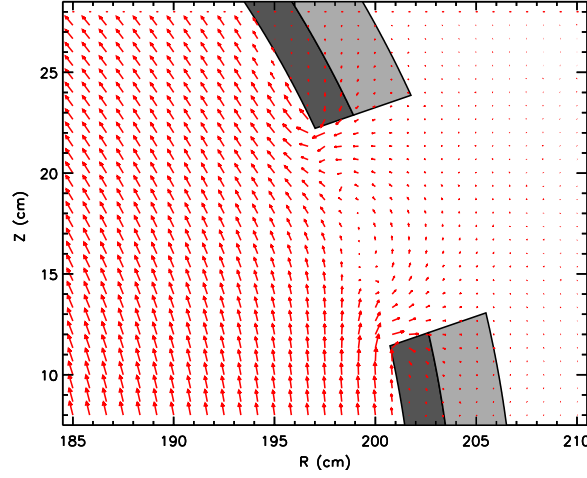


Figure 4. Poloidal magnetic field vectors in MST. The unperturbed field is produced by a MSTFit equilibrium reconstruction. R and Z are MST coordinates from figure 3. The darker shaded region corresponds to the diffusion region, as in figure 2.

and

$$\begin{aligned} \Delta B_\phi = \Phi_0 & \frac{(a_0 \cos(\theta) + R_0)(\phi - \phi_0)}{\pi \rho l^4} \frac{a^3}{\sqrt{1 - \left(\frac{a}{l}\right)^2}} \left[\frac{a + \rho}{l_p} - \frac{a - \rho}{l_n} \right] \\ & + \frac{B_{\phi_0}}{\pi} \operatorname{sgn}(r - a_0) \left[\frac{a}{l} \sqrt{1 - \left(\frac{a}{l}\right)^2} - \sin^{-1} \left(\frac{a}{l}\right) \right], \end{aligned} \quad (23)$$

with

$$\Phi_0(\mathbf{x}', t) = [B_{\phi_0}(t)(a_0 \cos(\theta) + R_0)(\phi - \phi_0) + B_{\theta_0}(t)a_0(\theta - \theta_0)] \times \operatorname{sgn}(r - a_0), \quad (24)$$

$$\rho(\phi, \theta) = \sqrt{a_0^2(\theta - \theta_0)^2 + (a_0 \cos(\theta) + R_0)^2(\phi - \phi_0)^2}, \quad (25)$$

$$l_p(\mathbf{x}') = \sqrt{(a + \rho)^2 + (r - a_0)^2}, \quad (26)$$

$$l_n(\mathbf{x}') = \sqrt{(a - \rho)^2 + (r - a_0)^2}, \quad (27)$$

and

$$l(\mathbf{x}') = \frac{1}{2}(l_p + l_n). \quad (28)$$

These perturbations are corrected for non-perfect conductivity in the shell by the same method as in (17), with stacking in the $+\hat{r}$ direction, to more accurately represent the physical system. The total perturbation is then

$$\Delta B_u = \frac{\sum_{n=1}^N \Delta B(a_0 \rightarrow a_0 - a_n) e^{-a_n/\delta}}{\sum_{n=1}^N e^{-a_n/\delta}}, \quad u \in \{x, y, z\}. \quad (29)$$

Figure 4 shows the poloidal magnetic field vectors near a 5.7 cm MST diagnostic port, with the same parameters as used in figure 2. The background field in this case is produced with a MSTFit equilibrium reconstruction [16] and is shown in figure 5.

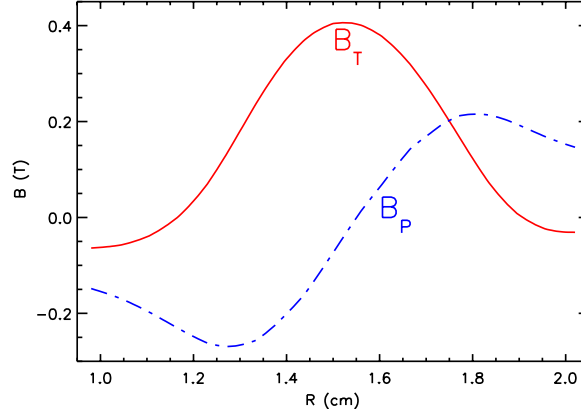


Figure 5. Reconstructed toroidal and poloidal equilibrium magnetic fields of MST used for figure 4. R is the MST major radius coordinate from figure 3.

4. Comparison with finite element calculation

To assess the affect of the field error of a single port on a purely toroidal vacuum magnetic field, a magnetostatic ANSYS finite element calculation was performed. The major radius of the toroidal configuration simulated was 1.5 m and the minor radius 0.47 m. A single 5.7 cm radius port was positioned at $(\phi_0, \theta_0) = (0^\circ, 0^\circ)$. The ANSYS solution was interpolated in both the θ and ϕ directions with a 0.5° resolution and the result was decomposed into the Fourier spectrum, given as

$$f(x) = \frac{a_0}{2} + \sum a_n \cos\left(\frac{n\pi x}{2}\right) + \sum b_n \sin\left(\frac{n\pi x}{2}\right), \quad (30)$$

with a_n as the Fourier cosine series coefficients and b_n as the Fourier sine series coefficients. This was then compared with the results of a Fourier decomposition of the analytic model.

Figures 6 and 7 show the Fourier spectrum in the toroidal and poloidal directions, respectively, 1 cm inboard from the port. For figure 6, the path of integration was located at $\theta = 0^\circ$, the center of the port, where the port field error in the radial direction is strongest. The field error is antisymmetric with respect to the port in the toroidal direction, leading to only nonzero b_n components of the spectrum. In figure 7, the path of integration was located at $\phi = 1.5^\circ$, near the edge of the port, where the port field error in the radial direction is strongest. The field error is symmetric with respect to the port in the poloidal direction, leading to only nonzero a_n components of the spectrum. In both cases, the agreement between the ANSYS calculation and the analytical model is very good. Small deviations between the FEM solution and the analytic model can be due to the uncertainty in the interpolated path for integration of the finite element grid. The grid has a mean node density of approximately 27 cm^{-3} , which causes the grid to be very coarse far from the port hole. By applying the symmetry of the system, we know that a_n in figure 6 and b_n in figure 7 must both identically be zero. Since the deviations in a_n and b_n in both figures are on the same order, we can assume that they are attributable to the same source.

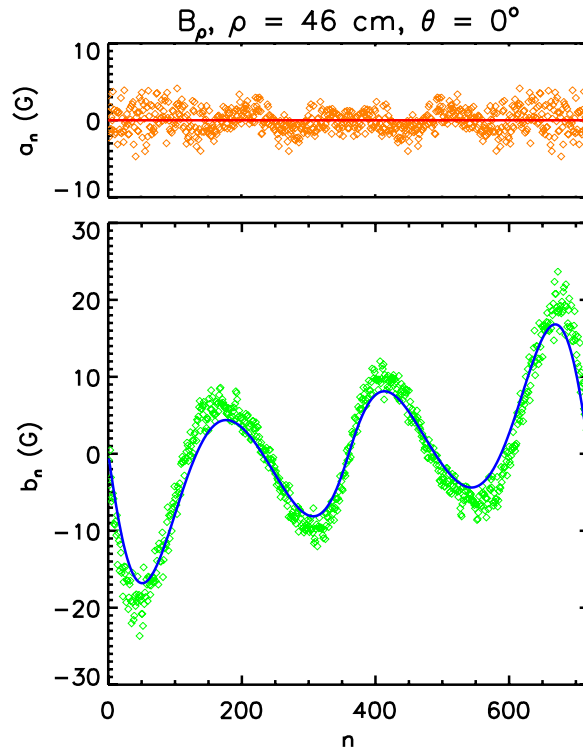


Figure 6. Fourier decomposition (in the toroidal, ϕ , direction of the effect of a single 5.7 cm radius port located at $(\rho_0, \phi_0, \theta_0) = (47 \text{ cm}, 0^\circ, 0^\circ)$) of the radial magnetic field. The integration path depicted passes through the center of the port in the toroidal direction, 1 cm inboard in the radial direction. The resolution in both the θ and ϕ directions is 0.5° and in the ρ direction is 1 cm. Solid lines indicate the analytic model prediction and symbols indicate the ANSYS calculation

5. Validation of the model

Experimental measurements have been made of the radial magnetic field of MST at a 5.7 cm radius diagnostic port when a toroidal field in vacuum is applied to the device. The magnetic field probe used contained seven tips arranged linearly and spaced at half inch intervals from the center of the port. Figure 8 shows comparisons between the model presented in section 3 and the radial field measurements for six angular probe orientations at a 0.4 cm insertion depth from the inner wall of MST toward the plasma region. Here, the skin depth is taken as 0.8 cm, corresponding to the rise rate of the MST toroidal field. These comparisons are made during the ramp phase of the toroidal field, 7.5 ms before the peak. Using the port coordinate system described by figure 1, measurements were performed with values of φ (the port azimuthal angle) of $0^\circ, 30^\circ, 60^\circ, 90^\circ, 120^\circ$ and 150° . These measurements are normalized to the measured toroidal field and the port radius. Each measurement and model pair is labeled with the angle relative to the port at which it was measured or calculated, and x'/a position is relative to the center of the port.

Figure 9 shows another comparison between the model and data. The probe array was aligned at $\varphi = 90^\circ$ and stepped into the plasma in 1 cm intervals. As the probe is moved deeper into the plasma, the measurements indicate that the perturbation field falls off as the model predicts. The inner surface of MST is located at $z' = 0$, positive z' values indicate

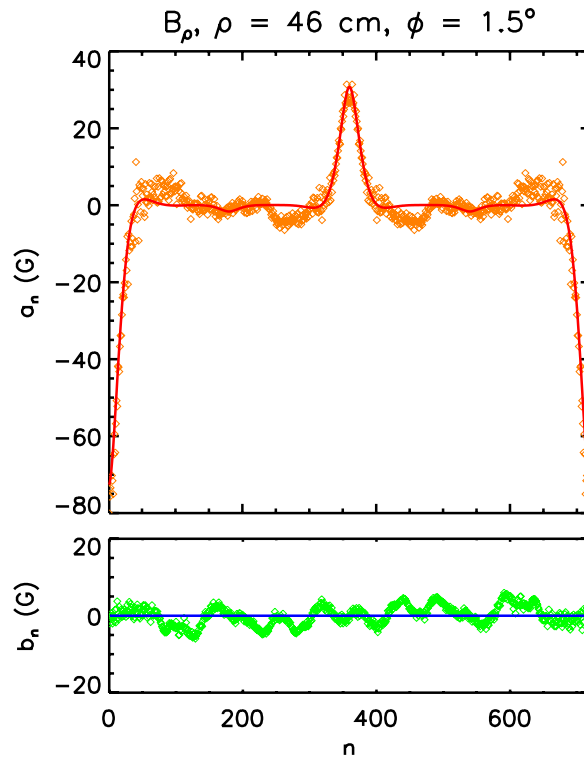


Figure 7. Fourier decomposition (in the poloidal, θ , direction of the effect of a single 5.7 cm radius port located at $(\rho_0, \phi_0, \theta_0) = (47 \text{ cm}, 0^\circ, 0^\circ)$) of the radial magnetic field. The integration path depicted passes near the edge of the port (at $\phi = 1.5^\circ$) in the poloidal direction, 1 cm inboard in the radial direction. As in figure 6 the resolution in both the θ and ϕ directions is 0.5° and in the ρ direction is 1 cm. Solid lines indicate the analytic model prediction and symbols indicate the ANSYS calculation.

probe insertion deeper within MST. As in figure 9, these comparisons are made 7.5 ms before the peak of the toroidal field. The data in both figures are shown as symbols and the model results are shown as lines. These figures show that the model is in good agreement with the measurements at each rotation angle and insertion depth.

6. HIBP trajectories with port field errors

The HIBP injects a singly charged (primary) ion beam into the plasma through a 2.5 cm radius (entrance) port and detects the doubly charged (secondary) ion beam at a 5.7 cm radius (exit) port. The port field errors have a cumulative effect on the beam trajectory, which causes displacement of the sample volume in the plasma and the impact location of the beam on the detector plane. The port field perturbation deflects all beam trajectories, but it is greatest when the beam passes near the edge of the port. Figure 10 shows two HIBP trajectories in the MST geometry, one through the edge regions of the entrance and exit ports and another through the center regions of the ports. Both the primary and secondary ion beams are shown. The port field error at the small HIBP entrance port is weaker than that of the exit port and acts on singly charged ions. The larger port field error due to the exit port, which also acts on doubly charged ions, will thus have a greater effect on the beam trajectory.

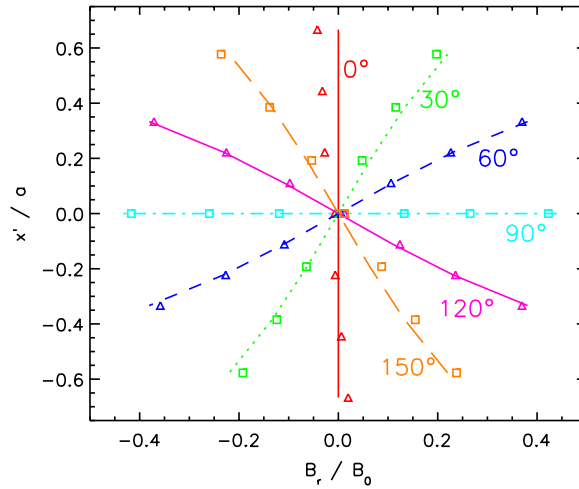


Figure 8. Model predictions (lines) and MST measurements made 4 mm inside the inner surface of MST at different probe insertion angles. x'/a (see figure 1) is relative to the center of the port. Lines indicate predictions and symbols indicate measurements.

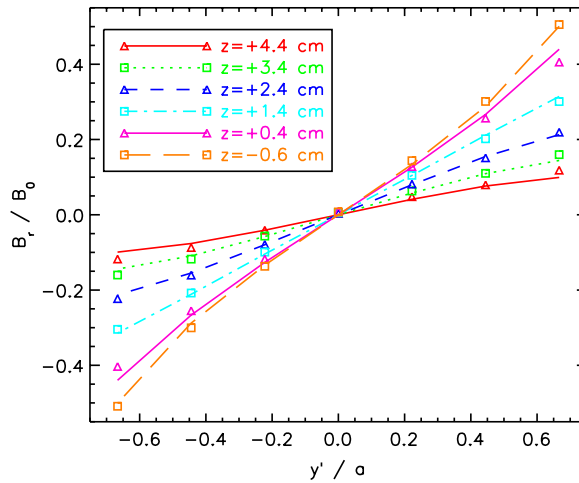


Figure 9. Model predictions (lines) and MST measurements made at various radial insertion distances at a $\varphi = 90^\circ$ rotation angle. y'/a (see figure 1) is relative to the center of the port. Lines indicate predictions and symbols indicate measurements.

Figure 11 shows the port perturbed (dashed lines) and unperturbed (solid lines) trajectories within the HIBP detection beamline. The detection beamline contains three pairs of electrostatic sweep plates (outlined and shaded in the figure) that redirect the secondary beam to the entrance apertures of an electrostatic analyzer (shown as gaps in the boundary at $z_{\text{SBL}} = 137$ cm). Each pair, (a)–(b) and (c)–(d), illustrates orthogonal projections of the beamline, with x_{SBL} largely in the toroidal direction and y_{SBL} in the poloidal direction.

The deflection of the beam at the rightmost electrostatic sweep plate pair is due to an applied sweep voltage. The upper pair (a)–(b) illustrates a simulation with the primary and secondary

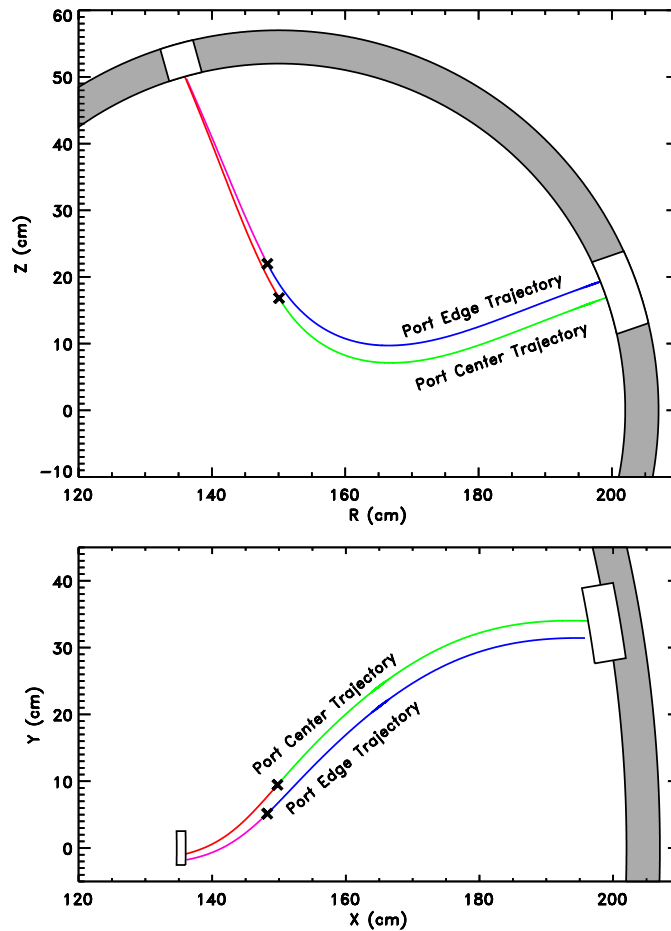


Figure 10. Poloidal (top) and toroidal (bottom) projections of HIBP trajectories through a MST plasma. The primary and secondary pairs for beams injected near the center and the edge of the entrance port through a magnetic field that includes the port field error. The x , y , R and z are MST coordinates, taken with the HIBP entrance port at $y = 0$. Crosses are used to designate the center of the sample volume locations (where the primary and secondary beams intersect).

beams passing near the center of the entrance and exit ports. In this case, the beam at the analyzer entrance aperture is displaced 0.88 cm in the \hat{x}_{SBL} (toroidal) direction from a trajectory calculated without inclusion of the port field error. When projected out to the detectors, this corresponds to a change of 1.20 cm. The combined poloidal and toroidal path variations move the sample volume (in MST coordinates) of $(|\Delta x|, |\Delta y|, |\Delta z|) = (0.20, 0.43, 0.34)$ cm, for a total change of 0.58 cm. The lower pair (c)–(d) illustrates the primary and secondary beams passing nearer the edges of the ports. The field error here is larger, but is strongest in the direction parallel to beam travel, and thus results in a smaller deflection. However, the position of the beam combined with the effect of the field error are sufficient to alter the trajectory from a non-detection in the no port field error case to a detection. To illustrate the smaller deviation due to the ports in this case, the combined poloidal and toroidal path variations move the sample volume (in MST coordinates) of $(|\Delta x|, |\Delta y|, |\Delta z|) = (0.20, 0.18, 0.39)$ cm, for a total change of 0.47 cm. A preliminary comparison of HIBP data (secondary ion currents on

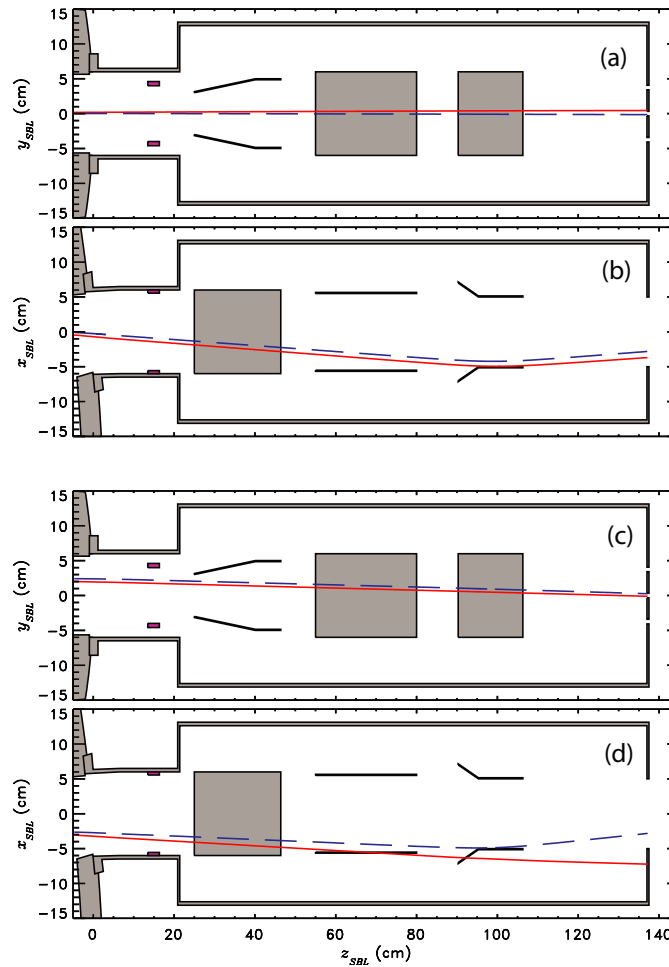


Figure 11. Poloidal (y_{SBL}) and toroidal (x_{SBL}) projections of beam trajectories through the HIBP detection beamline. Pair (a) and (b) is modeled with a beam passing nearer the center of the entrance and exit ports, and pair (c) and (d) with a beam passing nearer the edges of the ports. The x_{SBL} , y_{SBL} and z_{SBL} are HIBP coordinates, with the center of the exit port at $(x_{SBL}, y_{SBL}, z_{SBL}) = (0, 0, 0)$. Solid and dashed lines indicate, respectively, trajectories without and with the port error included.

the detectors) with trajectories computed with and without the port field error model suggests improved agreement when the port error is included.

Deviations on this order can have a significant affect on the interpretation of beam probe data. For accurate determination of electric potential and potential and density fluctuations, it is important to have the HIBP detections as near the center of the detector sets as possible. As shown by figures 11(c) and (d), the port field error can cause a change in trajectory calculation from non-detection to detection in some cases and in cases where there is a successful trajectory calculation with and without port field error, there is a significant motion (>1 cm) at the HIBP detectors. This is enough of a change in position to move the ion signal from being roughly centered on the detector to one side or the other. The motion of the sample volume due to the port field is likewise essential for accurate determination of the radial electric field from HIBP measurements.

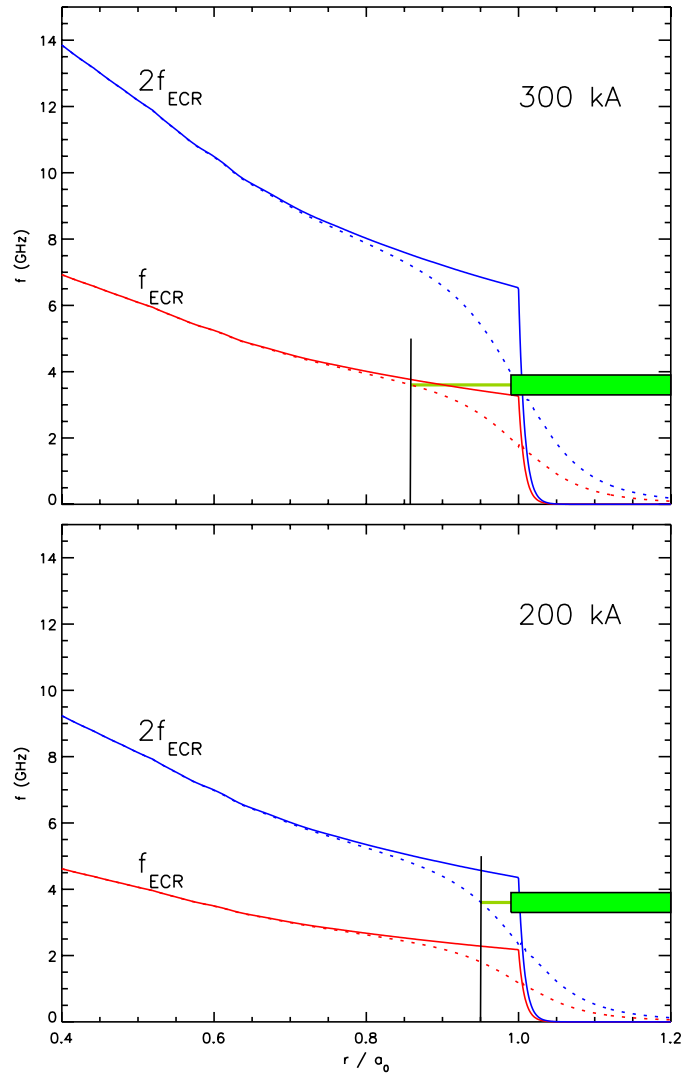


Figure 12. First (f_{ECR}) and second ($2f_{\text{ECR}}$) harmonic electron cyclotron resonance frequency profiles for equilibria at two plasma currents. Solid lines show profiles for unperturbed equilibria, dotted lines show the profiles for the corrected field. Also sketched is the EBW antenna at the 3.6 GHz launching frequency. The accessible region for 3.6 GHz launch is $r/a_0 > 0.86$ for the 300 kA case, while only $r/a_0 > 0.95$ for the 200 kA case.

7. EBW launch given port field errors

The distortion of the equilibrium magnetic field has significant implications on RF heating and current drive in MST. First, as a steep edge density profile is crucial to efficient coupling of the externally launched electromagnetic wave to the EBW [17], the perturbation of flux surfaces in the antenna near field has a deleterious effect on the coupling. Furthermore, even with the antenna retracted slightly behind the MST wall, a dielectric antenna cover acts as a limiter and modifies the local density profile in a fashion that improves coupling [18]. A second concern is that the magnetic field error from the large ($a/a_0 \approx 10\%$) port reduces accessibility as illustrated in figure 12. The EBW is strongly damped at the first or second

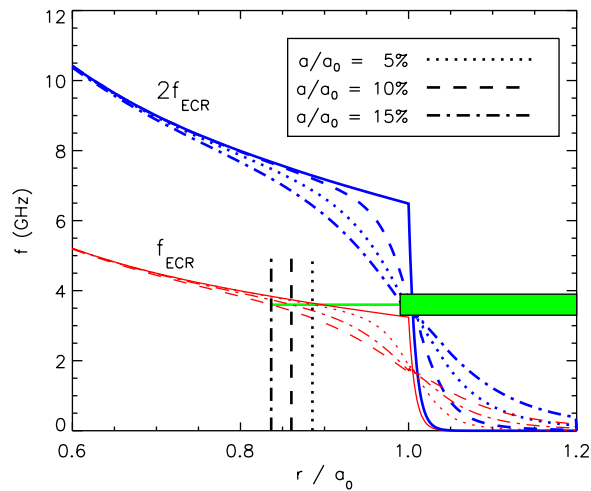


Figure 13. First (f_{ECR}) and second ($2f_{\text{ECR}}$) harmonic electron cyclotron resonance frequency profiles for a 300 kA equilibria. Solid lines show profiles for unperturbed equilibria, dotted and dashed lines show the profiles for the field when perturbations from various sized ports are included. Also sketched is the EBW antenna at the 3.6 GHz launching frequency, as well as vertical lines indicating the depth of penetration of the EBW layer for each port. The accessible region for 3.6 GHz launch is $r/a_0 > 0.89$ for the case of a port radius 5% of the minor radius, $r/a_0 > 0.86$ for a port radius 10% of the minor radius and $r/a_0 > 0.84$ for a port radius 15% of the minor radius.

harmonic of the electron cyclotron resonance, whose positions are determined by the strength of the magnetic field, $f_{\text{ECR}} = 27.9 \text{ GHz} \cdot |B|$. Considering an unperturbed equilibrium field, fundamental EBW heating for an optimized magnetic field strength allows resonant heating between $r/a_0 \approx 0.45$ and $r/a_0 \approx 0.99$, where access to the plasma core is blocked by the second harmonic resonance layer. Consideration of the total field (including port perturbation) alters the location of the first and second harmonic resonance layers, and the accessibility for optimized launch parameters is decreased from $r/a_0 \approx 0.79$ to $r/a_0 \approx 0.99$.

Figure 12 shows the effect of including the port field error in the calculation of the optimal EBW launching frequency and estimated deposition layer for 200 and 300 kA plasma current in MST. This suggests that for optimal deposition at a given launch frequency, the plasma current needs to be altered from that assumed by the unperturbed equilibrium. It also shows the dramatic decrease in size of the available deposition layer between the two harmonics. Figure 13 depicts the change in EBW deposition layer for three port radii. As the port radius increases, the depth of the EBW deposition layer increases. For ports with radii 5%, 10% and 15% of the machine minor radius, the EBW deposition penetrates to $r/a_0 = 0.89$, 0.86 and 0.84, respectively, for a plasma current of 300 kA. The 10% case approximates the experimental situation for the EBW antenna installed on MST.

Figure 14 shows the magnetic field contours for a 300 kA equilibrium located in the plane of the EBW system with the effect of the ports added. Near the ports shown in figure 14 it is apparent that the field error significantly alters the contours up to approximately one port diameter. One particularly important and initially overlooked feature is that for certain plasma conditions, the second harmonic for 3.6 GHz launch is not within the plasma, except for the region of reduced field due to the port hole. Second harmonic deposition then occurs in the antenna near field, far from the expected heating location. These effects on coupling and accessibility have been empirically observed, and with the present quantitative description of $|B|$, are being incorporated into planning of upcoming experimental campaigns.

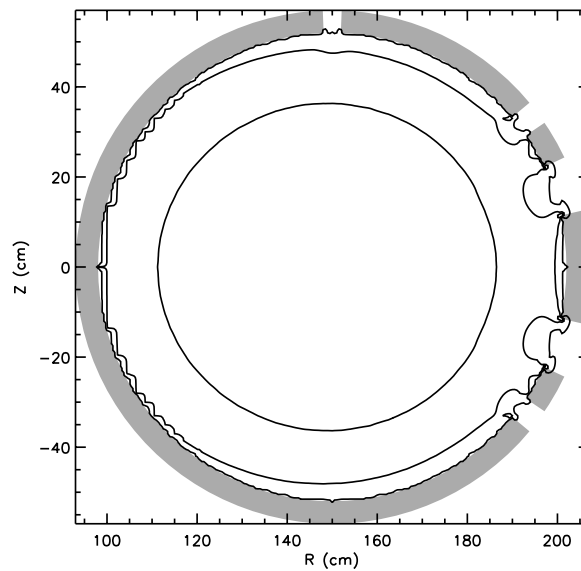


Figure 14. Magnetic field contours for a 300 kA equilibrium taking into account the port field errors of five ports: two 5.7 cm radius ports at $\pm 19^\circ$, two 2.54 cm radius ports at $\pm 37^\circ$ and one 1.905 cm radius port at 90° . R and Z here are MST coordinates. The field is strongly perturbed up to approximately one port diameter away from the port hole, recovering to the unperturbed state in the core of the plasma.

8. Summary and conclusions

In this paper, we have shown that port field errors are of considerable magnitude to affect several subsystems on MST and should be included in a comprehensive mean magnetic equilibrium reconstruction. The HIBP trajectories and sample volume location can be significantly affected by the passage through port field perturbations. An accurate calculation of the sample volume and detection location requires a reconstructed mean magnetic field that includes a port field error model. In addition, both the optimal launching frequency and the deposition layer contours for EBW heating are altered, suggesting new experimental operating conditions for upcoming campaigns.

In order to accurately model the perturbation due to a port in the conducting shell, an analytic solution for the perturbation has been developed and validated against measurements made on the MST RFP. This model is unique in that it aims to accurately represent the magnetic field effect in both the near-field and far-field regions. It can be readily adapted to any plasma confinement system with ports in a conducting wall and a time-changing magnetic field; so long as the port scale is smaller than the device scale, the unperturbed mean magnetic field is roughly constant over the port opening, and there is relatively low density near the conductor. The model shows excellent agreement with magnetic probe measurements taken near a 5.7 cm radius MST diagnostic port, as well as with finite element calculations.

Acknowledgments

The authors would like to acknowledge the assistance of many members of the MST experimental team, as well as the United States Department of Energy, for their support of this work.

References

- [1] Crowley T P 1994 *IEEE Trans. Plasma Sci.* **22** 291
- [2] Lei J *et al* 1999 *Rev. Sci. Instrum.* **70** 967
- [3] Den Hartog D J *et al* 2007 *Nucl. Fusion* **47** L17
- [4] Kerst D W 1962 *J. Nucl. Energy* **4** 253
- [5] Jernigan T, Rudmin J and Meade D M 1971 *Phys. Rev. Lett.* **26** 1298
- [6] Ohkawa T 1971 *Phys. Rev. Lett.* **27** 177
- [7] Almagri A F, Assadi S, Prager S C, Sarff J S and Kerst D W 1992 *Phys. Fluids B* **4** 4080
- [8] Rudmin J W and Drake J R 1977 *J. Appl. Phys.* **48** 1032
- [9] Howell R B and Vogel H F 1984 *J. Appl. Phys.* **56** 2017
- [10] Shinohara S 1988 *Japan. J. Appl. Phys.* **27** 1299
- [11] Saito K, Yoshida Z, Inoue N, Uesaka M and Hoshi Y 1988 *Japan. J. Appl. Phys.* **27** 1743
- [12] Masiello A, Yagi Y and Zollino G 1998 Estimation of field errors at the port holes of a reversed field pinch machine, TPE-RX Presented at the 13th Topical Meeting on the Technology of Fusion Energy (ANS) (Nashville, TN, 7–11 June 1998) *Fusion Technology* **34** (3 part 2) pp 553–7
- [13] Newton A A 1987 Magnetic field errors in reversed field pinches *Physics of Mirrors, Reversed Field Pinches and Compact Tori, Proceedings of the course and workshop (Varenna, Italy, 1–11 September 1987)* pp 221–40
- [14] Jackson J D 1998 *Classical Electrodynamics* 3rd edn (New York: Wiley)
- [15] Gradshteyn I S, Ryzhik I M, Jeffrey A and Zwillinger D 2007 *Table of Integrals, Series, and Products* (Burlington, MA: Academic)
- [16] Anderson J K, Forest C B, Biewer T M, Sarff J S and Wright J C 2004 *Nucl. Fusion* **44** 162
- [17] Cengher M 2005 47th Meeting of the APS Division of Plasma Physics (Orlando, FL, November 2005) BP1.00049
- [18] Anderson J K, Cox W and Forest C 2007 49th Meeting of the APS Division of Plasma Physics (Orlando, FL, November 2007) JP8.00134